International Forum on Aeroelasticity and Structural Dynamics
IFASD 2017
25-28 June 2017 Como, Italy

EFFICIENT REDUCED-ORDER MODELING FOR SKIN PANELS IN HYPERSONIC FLOW AND ITS APPLICATION TO GENERATING AEROTHERMOELASTIC SCALING LAWS

Daning Huang[1], **Tomer Rokita**[1], **Peretz P. Friedmann**[1]

[1]Department of Aerospace Engineering
The University of Michigan, Ann Arbor, MI, 48109

Keywords: Hypersonic aerothermoelasticity, scaling laws, reduced order modeling, linearized stability analysis

Abstract: This study describes the development of an efficient aerothermoelastic computational framework and its application to aerothermoelastic scaling law development. In the framework, a novel approach is developed for the reduced order model of the fluid solver, which accounts for non-uniform temperature distribution and geometrical scales using simple analytical pointwise models. The framework also features the linearized stability analysis and a tightly-coupled scheme, which are used for rapid aerothermoelastic simulation of extended flight time, and efficient identification of stability boundary. Subsequently, a new, two-pronged approach to aerothermoelastic scaling is presented. It combines the classical scaling approach with augmentation from numerical simulations of the specific problem. This enables one to obtain useful scaling information for important quantities that cannot be treated by the classical approach. Finally, the framework is applied to the development of a scaling law for a simple hypersonic skin panel configuration.

List of Symbols

Latin symbols

a, b	Panel dimensions
a_∞	Freestream sound speed
$\mathbf{a}, \mathbf{b}$	Structural and thermal modal coordinates
$\mathbf{C}$	Damping matrix of the structure
$\mathbf{C}_A$	Aerodynamic damping matrix
$\mathbf{C}_T$	Heat capacity matrix
$\mathbf{c}$	Flight conditions
c	Specific heat capacity
$\mathcal{D}$	Data sample set in the POD-kriging method
$D = \frac{Eh^3}{12(1-\nu^2)}$	Bending stiffness of a plate
$\mathbf{d}$	Input vector of the ROM
E	Young's modulus
$\mathbf{F}_I$	Internal force in the structure
$\mathbf{F}_S$	Structural loading
$\mathbf{f}$	Regression functions in kriging model

$\mathbf{f}_p^{cor}, \mathbf{f}_q^{cor}$	The correction models for pressure and heat flux
$\mathbf{H}$	Transformation matrix of an interpolation scheme
H, H_{aw}	Enthalpy
h	Panel thickness
$\mathbf{K}$	Tangent stiffness matrix
$\mathbf{K}_A$	Aerodynamic stiffness matrix
$\mathbf{K}_T$	Heat conduction matrix
L	Characteristic length
L_f	Upstream plate length
N_s	Number of samples
N_d	Input dimension of the ROM
N_y	Output dimension of the ROM
n_F	Number of parameters for flight conditions
n_S, n_T	Number of modes for structure and wall temperature
$\mathbf{M}$	Mass matrix
M	Mach number
$\mathbf{p}, p_i$	Vector of surface pressure and its ith entry
$Pr = \frac{\mu}{\rho\alpha}$	Prandtl number
$\mathbf{Q}_T$	Heat loading
$\dot{\mathbf{q}}, \dot{q}_i$	Vector of surface heat flux and its ith entry
q	Dynamic pressure
$\mathbf{r}, r_i$	Vector of correlation functions in kriging model and its ith entry
$\mathcal{R}$	Residue of a nonlinear equation
R	Universal gas constant
$Re = \frac{\rho V x}{\mu}$	Reynolds number
T	Temperature
$T_{cr} = \frac{\pi^2 h^2}{6\alpha(1+\nu)a^2}$	Critical temperature for thermal buckling of a plate
ΔT	Temperature increment in structure
$\mathbf{T}_w, T_{wi}$	Vector of wall Temperature and its ith entry
$\overline{T}_w$	Averaged wall Temperature
$\mathbf{T}$	Body Temperature
t	Time
t_I	The time when the system becomes unstable, considered as the stability boundary
$\mathbf{u}$	Structural displacement
$\mathbf{u}_F, u_{Fi}$	Vector of surface deformation and its ith entry
$\Delta\mathbf{u}$	Perturbation in structural displacements
V	Flow velocity
$\mathbf{y}$	Output vector of ROM

Greek symbols

α	Thermal expansion coefficient
$\alpha_f, \alpha_m, \bar{\beta}, \bar{\gamma}$	Coefficients in the generalized-α scheme
$\boldsymbol{\beta}$	Regression coefficients in kriging model
$\boldsymbol{\gamma}$	Correlation coefficients in kriging model
γ	Gas heat capacity ratio
δ	Boundary layer thickness

ζ	Damping of an aeroelastic mode
η	Heat transfer similarity parameter
θ	Incidence angle
κ^g, κ^s	Heat conductivity of gas and solid body
λ	Eigenvalue
$\tilde{\lambda} = \frac{q_\infty a^3}{DM_\infty}$	Nondimensional dynamic pressure
μ	Gas viscosity
$\mu_s = \frac{\rho_\infty a}{\rho h M_\infty}$	Mass ratio
ν	Poisson's ratio
ξ	Geometrical scale ratio
ρ	Air density
τ	Panel thickness to length ratio
$\mathbf{\Psi}$	A matrix with columns as modal vectors
ω	Frequency of an aeroelastic mode

Acronyms

ADflow	Automatic Differentiation flow solver
CFD	Computational Fluid Dynamics
GEP	Generalized Eigenvalue Problem
HYPATE	HYPersonic AeroThermoElasticity simulation environment
LCO	Limit Cycle Oscillation
LSA	Linearized Stability Analysis
PEP	Polynomial Eigenvalue Problem
POD	Proper Orthogonal Decomposition
ROM	Reduced Order Model

Subscripts / Superscripts

$\square^{EE}$	Quantities related to Eckert's reference enthalpy method
$\square^{E}$	Estimated quantity in the coupling scheme
$\square^{krg}$	Quantities related to kriging model
$\square^{LF}$	Quantities related to low-fidelity fluid solver
$\square^{PT}$	Quantities related to piston theory
$\square^{pk}$	Quantities related to POD-kriging model
$\square^{std}$	Quantities related to the steady quantity
$\square^{uns}$	Quantities related to the unsteady quantity
$\square_e$	Quantities at the edge of boundary layer
$\square_g$	Quantities associated with GEP
$\square_P$	Quantities related to POD modes
$\square_p$	Quantities associated with PEP
$\square_{ref}$	Quantities related to reference state
$\square_S$	Quantities related to structure
$\square_T$	Quantities related to thermal solution
$\square_\infty$	Quantities related to free stream state
$\square*$	Element-wise product of two vectors
$\dot{\square} = \frac{\partial \square}{\partial t}$	Time derivative
$conj(\square)$	Complex conjugate

1 INTRODUCTION, BACKGROUND AND OBJECTIVES

Driven by the interest in reusable launch vehicles for low-cost space exploration, as well as military applications, hypersonic flight has been an active area of research for decades [1]. Airbreathing hypersonic vehicles are exposed to extreme aerothermodynamic environments that involve high aerodynamic loading and heating, leading to degradation of material properties. The thermal stress introduced by the temperature gradients and geometrical constraints can dramatically affect structural integrity and cause structural instabilities, such as buckling, panel flutter, and control surface flutter. Therefore, the determination of aerothermoelastic stability boundary, i.e. the time elapsed before the onset of structural instability, is critical for the design of hypersonic vehicles.

One approach for determining the aerothermoelastic stability boundary is aerothermoelastic testing. Aerothermoelastic testing refers to the construction of a scaled version of the prototype vehicle and its direct insertion into a high-stagnation-temperature wind tunnel where the aerothermoelastic model can be exposed to aerodynamic heating and loading simultaneously. This approach is impractical for two reasons: (1) lack of appropriate wind tunnel facilities and (2) lack of aerothermoelastic scaling laws for constructing scaled models and mapping the experimental results back to the full scale prototype. Therefore, it is not surprising that design of airbreathing hypersonic vehicles has encountered numerous difficulties in the past, including failures during flight as well as high temperature structural testing. Work conducted on hypersonic vehicles in early 1960s has resulted in a landmark paper [2] where scaling laws for aerothermoelastic testing were derived for the cases when $M_\infty < 3.5$ and $T < 1000^\circ F$. However, modern hypersonic vehicles are expected to operate at much higher Mach numbers and in wider range of temperature. Therefore, it is necessary to extend the validity of aerothermoelastic scaling laws up to $M_\infty < 10$ and $T < 2500^\circ F$. Once such scaling laws were available, some of the flight tests on full-size vehicle could be replaced by experiments of scaled models, which could reduce the cost of hypersonic vehicle development by one or two orders of magnitude, and potentially shorten the design cycle of hypersonic vehicles.

In order to obtain new extended aerothermoelastic scaling laws, a two-pronged approach is adopted, which combines the classical approach used in [2] with modern simulation based on computational aerothermoelasticity. On one hand basic scaling requirements are established using dimensional analysis, in a manner that resembles the classical procedure. On the other hand, numerical simulations are used to generate "numerical similarity solutions" that can replace then analytical similarity solutions for refinement of the scaling laws [3]. The numerical similarity solutions require an extensive parametric study of computational aerothermoelastic solutions for different scales of geometric configurations and different combinations of flight conditions.

In the previous work [4], a computational framework, HYPersonic AeroThermoElasticity simulation environment (HYPATE), has been developed for numerical simulation of transient aerothermoelastic responses based on computational fluid dynamics (CFD). The HYPATE framework employs a partitioned approach with a loosely-coupled scheme. The fluid, thermal, and structural responses are computed by separate solvers and the coupling is achieved by exchanging boundary data at the interfaces of the domains once during each time step. The loosely-coupled scheme is shown to be numerically stable and second-order time accurate.

In a sequel to Ref. [4], reduced order modeling (ROM) techniques are applied to accelerate the fluid solver in the HYPATE framework [5]. The ROM takes advantage of the quasi-steady

nature of the hypersonic flow, i.e. the disparity of characteristic times of different physical domains: The fluid characteristic time is several orders of magnitude smaller than the structural characteristic time, and the structural characteristic time is several orders of magnitude smaller than the thermal characteristic time [6]. Therefore, in the ROM, the aerodynamic loading is modeled by combining a steady fluid solution with an unsteady contribution generated by piston theory. The steady fluid solution is modeled using the kriging method and proper orthogonal decomposition (POD), namely the POD-kriging method [7–9]. By using the ROM, the fluid solver is accelerated by five orders of magnitude for 3D applications, while maintaining the accuracy of a CFD solver [5].

In current study, three new features are introduced to the HYPATE framework to enable efficient parametric study of the aerothermoelastic stability boundary, so as to develop numerical similarity solutions.

The first feature is a novel methodology for the correction and scaling of a ROM. A POD-kriging ROM is generated from a sample set of high-fidelity fluid solutions, representing the aerodynamic loading and heating of a particular structural configuration. The ROM cannot be used to predict the aerodynamic loading and heating of a different structural configuration. Due to the intensive computational cost of generating the high-fidelity sample set, it is infeasible to generate a ROM for every possible geometric scale in the parametric study. Therefore, the new methodology for correction and scaling is introduced to improve the flexibility of the POD-kriging ROM. The methodology allows the extrapolation of a ROM to different geometric scales and flight conditions. So only *one* ROM is needed for the parametric study. It should be noted that, the new methodology is general and can be applied to ROM based on methods other than POD-kriging as well.

The second feature is an efficient tool for identifying the aerothermoelastic stability boundary. In the regular approach [10], the stability boundary is determined *after* the time domain simulation. The simulation is performed for a sufficient time span, so that the solution includes both the stable (quasi-steady) and unstable (oscillatory) structural response. The onset of the oscillation is considered the bifurcation stability boundary. In the new approach, the linearized stability analysis (LSA) is developed as an extension of the p-method in aeroelasticity [11]. The LSA is employed to examine the stability of the deformed structure at every time step. The simulation is terminated upon the onset of instability, thus there is no need to continue the simulation into the unstable region.

The last feature is introduced to overcome the limitations of the loosely-coupled scheme. The previous scheme was developed for general transient responses. However, the structural response before the onset of instability is quasi-steady, like the fluid solution. Therefore, a new tightly-coupled scheme is developed to utilize the quasi-steadiness of the response. The new scheme allows an order of magnitude larger time step than that in the previous scheme, and reduces the computational cost by an order of magnitude.

The objectives of the paper are:

1. To describe in detail three novel features that have been introduced in the HYPATE framework. These are:
   (a) A novel approach for correction and scaling of a ROM based on the POD-kriging method to determine aerodynamic loading and heating on a particular configuration including a provision for modifying its geometrical scale.

(b) A new approach for determining the time required for the onset of instability in hypersonic flight using a linearized approach that requires computing the system response only until the onset of instability and avoid the need for calculating system response beyond this point.
(c) A new approach that allows extremely efficient implementation of the tightly-coupled scheme due to an order of magnitude increase in the time step size.

2. The second objective of the paper is to illustrate a novel two-pronged approach for developing aerothermoelastic scaling laws by its application to a simple three-dimensional panel in hypersonic flow.

2 REDUCED ORDER MODELING FOR THE FLUID SOLVER

The fluid solver produces the pressure $\mathbf{p}$ and heat-flux $\dot{\mathbf{q}}$ on the structural surface given the surface deformation $\mathbf{u}_F$, surface velocity $\dot{\mathbf{u}}_F$, wall temperature $\mathbf{T}_w$, and the flight condition $\mathbf{c}$,

$$\mathbf{c} = [M_\infty, p_\infty, T_\infty]^T \tag{1}$$

The ROM for the fluid solver employs the assumption that the flow is quasi-steady, which leads to two approximations. First, the pressure is weakly coupled with structural velocity, indicating that it can be decomposed into steady and unsteady components and modeled separately.

$$\mathbf{p}(\mathbf{c}, \mathbf{u}_F, \dot{\mathbf{u}}_F, \mathbf{T}_w) = \mathbf{p}^{std}(\mathbf{c}, \mathbf{u}_F, \mathbf{T}_w) + \mathbf{p}^{uns}(\mathbf{c}, \mathbf{u}_F, \dot{\mathbf{u}}_F) \tag{2}$$

Secondly, the surface heat-flux is independent of any terms associated with time derivatives, including structural velocity.

$$\dot{\mathbf{q}}(\mathbf{c}, \mathbf{u}_F, \dot{\mathbf{u}}_F, \mathbf{T}_w) = \dot{\mathbf{q}}(\mathbf{c}, \mathbf{u}_F, \mathbf{T}_w) \tag{3}$$

The quantities $\mathbf{p}^{std}$ and $\dot{\mathbf{q}}$ are modeled using the POD-kriging method combined with the correction and scaling methodology. The quantity $\mathbf{p}^{uns}$ is the unsteady correction and is modeled using piston theory.

In the following, the building blocks of the fluid ROM are presented. First, the basic modeling tools, which are the POD-kriging method and the analytical models for hypersonic aerodynamics, are described. Then, the strategy for utilizing these tools for an efficient fluid ROM is presented.

2.1 The Basic Modeling Tools

2.1.1 The POD-kriging method

In the POD-kriging method, a nonlinear interpolation model for the problem is constructed from a set of data sample points $\mathcal{D} = \{\mathbf{d}_i, \mathbf{y}_i\}_{i=1}^{N_s}$, where input vector $\mathbf{d} \in \mathbb{R}^{N_d}$ and output vector $\mathbf{y} \in \mathbb{R}^{N_y}$.

In the context of a fluid ROM, the input vector typically contains $N_d = 10 \sim 20$ parameters characterizing $\mathbf{c}$, $\mathbf{u}_F$, and $\mathbf{T}_w$. The Optimal Latin Hypercube (OLH) sampling method is used to generate uniformly and randomly distributed sample inputs in the parameter space of interest. The output vector can be the steady component of the pressure $\mathbf{p}^{std}$ or the heat-flux $\dot{\mathbf{q}}$. Its dimension depends on the discretization of the wall boundary of the fluid domain, which is

typically of the order of $N_y = 10^3 \sim 10^4$. Direct interpolation between the input and output vectors can be computationally intensive.

Therefore, in the POD-kriging method, proper orthogonal decomposition is used to generate a low-dimensional yet accurate approximation of the output vector. The snapshot method [12] is applied to the output vectors to extract the POD modes $\mathbf{\Psi}_P$, which represent the dominating patterns in the output vectors. Then the output vector $\mathbf{y}$ and its POD component $\mathbf{y}_P \in \mathbb{R}^{N_P}$ are related by POD transformation,

$$\mathbf{y}_P = \mathbf{\Psi}_P^T \mathbf{y}, \quad \mathbf{y} \approx \mathbf{\Psi}_P \mathbf{y}_P \tag{4}$$

The number of POD modes N_P, that are required for an accurate representation, is typically less than 20, much smaller than N_y.

Then, the kriging method [13] is used to construct a nonlinear interpolation model between $\mathbf{d}$ and $\mathbf{y}_P$. The model is characterized by two terms,

$$\mathbf{y}^{krg}(\mathbf{d}) = \boldsymbol{\beta}^T \mathbf{f}(\mathbf{d}) + \boldsymbol{\gamma}^T \mathbf{r}(\mathbf{d}) \tag{5}$$

The first term in Eqn. (5) is a regression function representing the global trend of the unknown function. In current study, the regression function employs polynomials up to second order,

$$\mathbf{f}(\mathbf{d}) = [1, d_1, \cdots, d_{N_d}, d_1^2, \cdots, d_1 d_{N_d}, d_2^2, \cdots, d_2 d_{N_d}, \cdots, d_{N_d}^2] \tag{6}$$

The second term in Eqn. (5) is a correlation function representing the local deviation of the regression function to the actual sample data. Typically a Gaussian kernel is used as the correlation function.

$$r_i(\mathbf{d}) = \exp\left[-(\mathbf{d}_i - \mathbf{d})^T \mathbf{\Theta} (\mathbf{d}_i - \mathbf{d})\right], \quad i = 1, \cdots, N_s \tag{7}$$

where $\mathbf{\Theta}$ is a diagonal coefficient matrix. The coefficients $\boldsymbol{\beta}$ and $\boldsymbol{\gamma}$ in Eqn. (5) are determined from the sample data set using standard algorithms [13].

Combining Eqns. (4) and (5), the POD-kriging model for the data set $\mathcal{D}$ is,

$$\mathbf{y}^{pk}(\mathbf{d}) = \mathbf{\Psi}_P \mathbf{y}^{krg}(\mathbf{d}) \tag{8}$$

and its Jacobian w.r.t. the input is,

$$\frac{\partial \mathbf{y}^{pk}}{\partial \mathbf{d}} = \mathbf{\Psi}_P \frac{\partial \mathbf{y}^{krg}}{\partial \mathbf{d}} = \mathbf{\Psi}_P \boldsymbol{\beta}^T \frac{\partial \mathbf{f}}{\partial \mathbf{d}} + \mathbf{\Psi}_P \boldsymbol{\gamma}^T \frac{\partial \mathbf{r}}{\partial \mathbf{d}} \tag{9}$$

where the Jacobians $\frac{\partial \mathbf{f}}{\partial \mathbf{d}}$ and $\frac{\partial \mathbf{r}}{\partial \mathbf{d}}$ can be computed analytically from Eqns. (6) and (7).

A noteworthy issue of the POD-kriging method, or any other interpolation methods, is the curse of dimensionality. The sample data for generating the model should cover the parameter space of interest. Using OLH sampling method, the requirement of coverage causes the number of samples to grow exponentially with the number of input N_d, which would dramatically increase the computational cost for ROM generation. Sometimes a large number of input causes the failure of the convergence of the ROM. Therefore, N_d should be small enough for computational efficiency, yet large enough for flexibility of the ROM.

2.1.2 The analytical models

Analytical models provide pointwise models for the pressure and the heat-flux. That means the fluid solution at a point only depends on the properties of the wall boundary and the freestream at the same point.

In the inviscid limit, the aerodynamic pressure over a panel is well approximated by the third-order piston theory [14],

$$p^{PT}(u_F, \dot{u}_F) = p_\infty \left[\gamma M_n + \frac{\gamma(\gamma+1)}{4} M_n^2 + \frac{\gamma(\gamma+1)}{12} M_n^3\right] \tag{10}$$

where,

$$M_n = M_\infty u_{F,x} + \frac{\dot{u}_F}{a_\infty} \tag{11}$$

The piston theory has been used to formulate the unsteady component of the pressure in Eqn. (2) [15],

$$p_i^{uns}(u_{Fi}, \dot{u}_{Fi}) = p^{PT}(u_{Fi}, \dot{u}_{Fi}) - p^{PT}(u_{Fi}, \dot{u}_{Fi} = 0) \tag{12}$$

The formulation is applicable to any flight conditions and geometric scales, and is independent of the wall temperature.

Assuming that the boundary layer is fully turbulent, the aerodynamic heat flux is computed using Eckert's reference enthalpy method [16],

$$\dot{q}^{EE}(u_F, T_w) = St(T_r)\rho(T_r)V_e[H_{aw}(T_r) - H(T_w)] \tag{13}$$

where the enthalpy H, air density ρ, and Stanton number St are temperature dependent,

$$St(T) = \frac{0.185}{Pr(T)^{2/3}} \left[\log_{10} \frac{\rho(T)V_e x}{\mu(T)}\right]^{-2.584} \tag{14}$$

$$H_{aw}(T) = H(T_e) + Pr(T)^{1/3} \frac{V_e^2}{2} \tag{15}$$

and the reference temperature T_r satisfies,

$$H(T_r) = H(T_e) + 0.50[H(T_w) - H(T_e)] + 0.22[H_{aw}(T_r) - H(T_e)] \tag{16}$$

At the edge of the boundary layer, the pressure $p_e = p^{PT}(u_F, 0)$, and the other flow properties T_e and V_e satisfy,

$$\frac{T_e}{T_\infty} = \left(\frac{p_e}{p_\infty}\right)^{\frac{\gamma-1}{\gamma}} = \frac{1 + \frac{\gamma-1}{2}M_\infty^2}{1 + \frac{\gamma-1}{2}M_e^2}, \quad V_e = M_e\sqrt{\gamma R T_e} \tag{17}$$

2.2 The Modeling Strategy

2.2.1 The limitations in the conventional ROM

In previous studies [7–9], the steady component of the pressure $\mathbf{p}^{std}$, and the-heat flux $\dot{\mathbf{q}}$ are modeled using the POD-kriging method directly. An extensive list of input parameters has to be included in the POD-kriging models to account for a range of flight conditions of interest, structural deformation, and non-uniform wall temperature distribution. The flight conditions

include n_F parameters, such as M_∞ and T_∞. The structural deformation and the wall temperature are represented using a linear combination of n_S structural modes and n_T thermal modes, respectively,

$$\mathbf{u}_F = \mathbf{\Psi}_S \mathbf{a} \tag{18}$$

$$\mathbf{T}_w = \mathbf{\Psi}_T \mathbf{b} \tag{19}$$

Then, the conventional POD-kriging models are

$$\mathbf{p}^{std}(\mathbf{c}, \mathbf{u}_F, \mathbf{T}_w) = \mathbf{p}^{pk}(\mathbf{d}) \tag{20}$$

$$\dot{\mathbf{q}}(\mathbf{c}, \mathbf{u}_F, \mathbf{T}_w) = \dot{\mathbf{q}}^{pk}(\mathbf{d}) \tag{21}$$

where the input vector for this approach has $(n_F + n_S + n_T)$ entries,

$$\mathbf{d}^T = [\mathbf{c}^T, \mathbf{a}^T, \mathbf{b}^T] = [\mathbf{c}^T, \mathbf{u}_F^T \mathbf{\Psi}_S, \mathbf{T}_w^T \mathbf{\Psi}_T] \tag{22}$$

The conventional POD-kriging model has three limitations. First, it is only suitable for a fixed geometrical configuration, which is a direct result of the sample data set that is generated for a particular geometrical configuration. The second limitation is the curse of dimensionality, caused by the numerous parameters needed for the flight conditions and the wall temperature. The third limitation is due to the *a priori* assumption on the form of the wall temperature, which usually proves to be too simplistic for the actual distribution [17].

An alternative approach, which relieves the curse of dimensionality, is to generate a POD-kriging model where the wall temperature distribution is characterized by the average temperature $\overline{T}_w$ [17]. Then, the POD-kriging model for the heat-flux has to be augmented by a correction model,

$$\dot{\mathbf{q}}(\mathbf{c}, \mathbf{u}_F, \mathbf{T}_w) = \mathbf{f}_q^{cor}(\mathbf{c}, \mathbf{T}_w) * \dot{\mathbf{q}}^{pk}(\mathbf{d}) \tag{23}$$

where now the input vector now has only $(n_F + n_S + 1)$ entries,

$$\mathbf{d}^T = [\mathbf{c}^T, \mathbf{a}^T, \overline{T}_w] \tag{24}$$

The correction model accounts for the discrepancy between the average temperature and the actual non-uniform temperature distribution. Previous studies [17] have suggested a pointwise correction based on Chapman–Rubesin [18] solution of laminar flow over a flat surface, with generalization for turbulent flow. However, this approach relies on the tuning of empirical coefficients that depends on flight conditions and geometrical configurations.

2.2.2 The methodology for ROM correction and scaling

A novel methodology for correction and scaling is developed in order to overcome the three limitations of the conventional POD-kriging method discussed in the previous section. In particular, the novel approach corrects the ROM for different geometrical scales, so that the ROM can be applied to the development of aerothermoelastic scaling laws.

First, the POD-kriging models for aerodynamic pressure and heat-flux are generated for *fixed* reference flight conditions $\mathbf{c}_{ref}$, *uniform* wall temperature $\overline{T}_w$, and a *fixed* geometrical configuration with a characteristic length L_{ref}. Then, the models are corrected to account for both

non-uniform temperature distribution and for extrapolation to different flow conditions or geometrical scale. The correction for a scaled configuration with a characteristic length L, at arbitrary flight condition $\mathbf{c}$, and with an arbitrary non-uniform wall temperature distribution $\mathbf{T}_w$ has the following form,

$$\mathbf{p}^{std}(\mathbf{c}, \mathbf{u}_F, \mathbf{T}_w; L) = \mathbf{f}_p^{cor}(\mathbf{c}, \mathbf{u}_F, \mathbf{T}_w, \xi) * \mathbf{p}^{pk}(\mathbf{d}) \tag{25}$$

$$\dot{\mathbf{q}}(\mathbf{c}, \mathbf{u}_F, \mathbf{T}_w; L) = \mathbf{f}_q^{cor}(\mathbf{c}, \mathbf{u}_F, \mathbf{T}_w, \xi) * \dot{\mathbf{q}}^{pk}(\mathbf{d}) \tag{26}$$

where $\xi = L_{ref}/L$ is the geometrical scale ratio. The input vector for this approach is reduced to $(n_S + 1)$ entries:

$$\mathbf{d}^T = [\xi \mathbf{a}^T, \overline{T}_w] \tag{27}$$

The correction is based on recognizing that, while the analytical models do not provide as accurate *absolute* results as the high-fidelity CFD, they capture the trends with respect to the input parameters with sufficient accuracy. Therefore, the *ratio* of two analytical solutions, at two different states, can be used as a correction factor. Utilizing this concept with piston theory and Eckert's reference enthalpy, for pressure and heat-flux respectively, yields the following pointwise correction:

$$f_{pi}^{cor}(\mathbf{c}, u_{Fi}, T_{wi}, \xi) = \frac{p_i^{std}(\mathbf{c}, u_{Fi}, T_{wi}; L)}{p_i^{pk}(\mathbf{d})} \approx \frac{p^{PT}(\mathbf{c}, u_{Fi})}{p^{PT}(\mathbf{c}_{ref}, \xi u_{Fi})} \approx \frac{q_\infty \sqrt{M_{ref}^2 - 1}}{q_{ref} \sqrt{M_\infty^2 - 1}} \tag{28}$$

$$f_{qi}^{cor}(\mathbf{c}, u_{Fi}, T_{wi}, \xi) = \frac{\dot{q}(\mathbf{c}, u_{Fi}, T_{wi}; L)}{q_i^{pk}(\mathbf{d})} \approx \frac{\dot{q}^{EE}(\mathbf{c}, u_{Fi}, T_{wi})}{\dot{q}^{EE}(\mathbf{c}_{ref}, \xi u_{Fi}, \overline{T}_w)} \tag{29}$$

where f_{pi}^{cor} and f_{qi}^{cor} stands for pressure and heat-flux corrections for the i^{th} node.

The correction takes care of the discrepancy in the wall temperature and flight conditions without introducing any empirical coefficients. Moreover, the models takes into account of the geometrical scaling with the new parameter ξ. Such a correction is beneficial, as it (1) expands the applicability of a certain ROM to a wider range of applications, and (2) dramatically reduces the cost for ROM generation, by reducing the required number of input parameters and subsequently the number of samples.

2.2.3 Final form of the fluid ROM

The final form of the fluid ROM is,

$$\mathbf{p}(\mathbf{c}, \mathbf{u}_F, \dot{\mathbf{u}}_F, \mathbf{T}_w) = \mathbf{f}_p^{cor}(\mathbf{c}, \mathbf{u}_F, \xi) * \mathbf{p}^{pk}(\mathbf{d}) + \mathbf{p}^{uns}(\mathbf{c}, \mathbf{u}_F, \dot{\mathbf{u}}_F) \tag{30}$$

$$\dot{\mathbf{q}}(\mathbf{c}, \mathbf{u}_F, \dot{\mathbf{u}}_F, \mathbf{T}_w) = \mathbf{f}_q^{cor}(\mathbf{c}, \mathbf{u}_F, \xi) * \dot{\mathbf{q}}^{pk}(\mathbf{d}) \tag{31}$$

where $\mathbf{d}$ is defined by Eqn. (27).

The Jacobians of the pressure w.r.t. to the displacement and the velocity are,

$$\frac{\partial \mathbf{p}}{\partial \mathbf{u}_F} = \frac{q_\infty \sqrt{M_{ref}^2 - 1}}{q_{ref} \sqrt{M_\infty^2 - 1}} \frac{\partial \mathbf{p}^{pk}(\mathbf{d})}{\partial \mathbf{d}} \frac{\partial \mathbf{d}}{\partial \mathbf{u}_F} \tag{32}$$

$$\frac{\partial \mathbf{p}}{\partial \dot{\mathbf{u}}_F} = \frac{\partial \mathbf{p}^{uns}(\mathbf{c}, \mathbf{u}_F, \dot{\mathbf{u}}_F)}{\partial \dot{\mathbf{u}}_F} \tag{33}$$

3 THE COMPUTATIONAL FRAMEWORK

3.1 The Governing Equations

Aerothermoelastic simulation involves in the numerical solutions in the solid and the fluid domains, with an interface at the fluid-solid boundary for information exchange.

3.1.1 The fluid solver

Three fluid solvers are developed for different levels of fidelity. The low-fidelity fluid solver is based on analytical models, i.e. the piston theory from Eqn. (10) and Eckert's reference enthalpy method from Eqn. (13).

$$p_i^{LF}(\mathbf{u}_F, \dot{\mathbf{u}}_F, \mathbf{T}_w) = p^{PT}(u_{Fi}, \dot{u}_{Fi}) \tag{34}$$

$$\dot{q}_i^{LF}(\mathbf{u}_F, \dot{\mathbf{u}}_F, \mathbf{T}_w) = \dot{q}^{EE}(u_{Fi}, T_{wi}) \tag{35}$$

The next level up is a ROM-based fluid solver that has higher fidelity. The ROM-based fluid solver is the primary means for the reduction of computational cost in the hypersonic aerothermoelastic simulation. The formulation is given by Eqns. (30) and (31).

The high-fidelity fluid solver is the CFD solver, which is based on ADflow (Automatic Differentiation flow solver) [19]. The ADflow code is a highly-parallelized, multiblock, finite volume solver. The Arbitrary Lagrangian-Eulerian formulation is implemented in ADflow for problems with moving boundary [4]. The Spalart-Allmaras turbulence model and perfect gas model are employed for hypersonic aerodynamics. The usage of the CFD solver is limited due to its high computational cost. In current study, the CFD solver is used to generate data samples for the ROM solver.

3.1.2 The structural solver

The structural solver is based on a finite element model for anisotropic doubly curved shallow shells, with shear, thermal stress, geometric and material nonlinearities [4]. The governing equation is,

$$\mathbf{M}\ddot{\mathbf{u}} + \mathbf{C}\dot{\mathbf{u}} + \mathbf{F}_I(\mathbf{u}, \mathbf{T}) = \mathbf{F}_S \tag{36}$$

where $\mathbf{F}_S$ is the aerodynamic loading passed from the fluid domain to the solid domain.

Equation (36) is discretized in time using the generalized-α scheme [20],

$$\mathcal{R}_S^{Dyn}(\mathbf{u}^{n+1}) = \mathbf{M}\ddot{\mathbf{u}}^{n+1} + \mathbf{C}\dot{\mathbf{u}}^{n+1} + \mathbf{F}_I(\mathbf{u}^{n+1}, \mathbf{T}^{n+1}) = \mathbf{F}_S^{n+1} \tag{37}$$

where,

$$\begin{aligned}
\mathbf{u}^{n+1} &= (1-\alpha_f)[\mathbf{u}^n + \Delta t\dot{\mathbf{u}}^n + (1-2\bar{\beta})\frac{\Delta t^2}{2}\ddot{\mathbf{u}}^n + \bar{\beta}\Delta t^2\ddot{\mathbf{u}}^{n+1}] + \alpha_f\ddot{\mathbf{u}}^n \\
\dot{\mathbf{u}}^{n+1} &= (1-\alpha_f)[\dot{\mathbf{u}}^n + (1-\bar{\gamma})\Delta t\ddot{\mathbf{u}}^n + \bar{\gamma}\Delta t\ddot{\mathbf{u}}^{n+1}] + \alpha_f\dot{\mathbf{u}}^n \\
\ddot{\mathbf{u}}^{n+1} &= (1-\alpha_m)\ddot{\mathbf{u}}^{n+1} + \alpha_m\ddot{\mathbf{u}}^n
\end{aligned}$$

The generalized-α scheme is an extension of the Newmark-β scheme [21] and the HHT-α scheme [22]. The generalized-α scheme provides controllable numerical dissipation that damps

out spurious high-frequency response due to the finite element formulation [20]. For second-order time accuracy and unconditional stability (in the linear sense), the parameters are chosen as,

$$\alpha_f = 0.05, \quad \alpha_m = 0, \quad \bar{\gamma} = \frac{1}{2} - \alpha_m + \alpha_f, \quad \bar{\beta} = \frac{1}{4}(1 - \alpha_m + \alpha_f)^2$$

When the structural response is quasi-steady, the velocity and the acceleration are assumed to be negligible, and the governing equation Eqn. (36) simplifies to,

$$\mathcal{R}_S^{Sta}(\mathbf{u}^{n+1}) = \mathbf{F}_I(\mathbf{u}^{n+1}, \mathbf{T}^{n+1}) = \mathbf{F}_S^{n+1} \tag{38}$$

In Eqns. (37) and (38), the governing equations for the structural solver are expressed in the residue form,

$$\mathcal{R}_S(\mathbf{u}) = \mathbf{F}_S^{n+1} \tag{39}$$

Equation (39) is solved using the Newton-Raphson method.

$$\begin{cases} \left(\frac{\partial \mathcal{R}_S}{\partial \mathbf{u}^i} - \frac{\partial \mathbf{F}_S^{n+1}}{\partial \mathbf{u}^i} - \frac{\partial \mathbf{F}_S^{n+1}}{\partial \dot{\mathbf{u}}^i}\frac{\partial \dot{\mathbf{u}}^i}{\partial \mathbf{u}^i}\right)\Delta \mathbf{u} = -(\mathcal{R}_S(\mathbf{u}^i) - \mathbf{F}_S^{n+1}) \\ \mathbf{u}^{i+1} = \mathbf{u}^i + \Delta \mathbf{u} \end{cases} \tag{40}$$

where $i \geq 0$ is the iteration step and $\mathbf{u}^0$ is the initial guess for the $n+1$ time step. The iteration procedure converges when the norm of the residue $||\mathcal{R}_S(\mathbf{u}^{i+1})||$ is smaller than a prescribed tolerance.

3.1.3 The thermal solver

The heat transfer in the solid domain is based on a finite element model using a layer-wise thermal lamination theory for composite shells. The governing equation is,

$$\mathbf{C}_T(\mathbf{T})\dot{\mathbf{T}} + \mathbf{K}_T(\mathbf{T})\mathbf{T} = \mathbf{Q}_T \tag{41}$$

where $\mathbf{C}_T$ and $\mathbf{K}_T$ are temperature-dependent due to material nonlinearity, and $\mathbf{Q}_T$ is the aerodynamic heating passed from the fluid domain to the solid domain.

Equation (36) is temporally discretized using the Crank-Nicolson scheme [23],

$$\mathcal{R}_T(\mathbf{T}^{n+1}) = \mathbf{C}_T(\mathbf{T}^{n+\frac{1}{2}})\dot{\mathbf{T}}^{n+\frac{1}{2}} + \mathbf{K}_T(\mathbf{T}^{n+\frac{1}{2}})\mathbf{T}^{n+\frac{1}{2}} = \mathbf{Q}_T^{n+\frac{1}{2}} \tag{42}$$

where,

$$\mathbf{T}^{n+\frac{1}{2}} = \frac{1}{2}(\mathbf{T}^n + \mathbf{T}^{n+1})$$
$$\dot{\mathbf{T}}^{n+\frac{1}{2}} = \frac{1}{\Delta t}(\mathbf{T}^{n+1} - \mathbf{T}^n)$$

Similar to the structural solver, Eqn. (42) is solved using Newton-Raphson method,

$$\begin{cases} \frac{\partial \mathcal{R}_T}{\partial \mathbf{T}^i}\Delta \mathbf{T} = -(\mathcal{R}_T(\mathbf{T}^i) - \mathbf{Q}_T^{n+1}) \\ \mathbf{T}^{i+1} = \mathbf{T}^i + \Delta \mathbf{T} \end{cases} \tag{43}$$

3.1.4 The fluid-solid boundary

At the fluid-solid boundary, the discretizations of the solid and the fluid surfaces do not match. Usually, the nodes of fluid mesh are denser than those of the solid mesh. Therefore, interpolation schemes are needed for information exchange between the solid and the fluid domains. The displacements $\mathbf{u}$ and the temperature $\mathbf{T}$ are interpolated from the solid mesh to the fluid mesh using the finite element scheme [24]. The aerodynamic loading $\mathbf{p}$ and heat flux $\dot{\mathbf{q}}$ are interpolated from the fluid mesh to the solid mesh using the quadrature-projection scheme [25]. The mathematical forms of the interpolation schemes are expressed as linear transformations,

$$\mathbf{F}_S = \mathbf{H}_{SF}\mathbf{p} \tag{44}$$

$$\mathbf{Q}_T = \mathbf{H}_{TF}\dot{\mathbf{q}} \tag{45}$$

$$\mathbf{u}_F = \mathbf{H}_{FS}\mathbf{u} \tag{46}$$

$$\mathbf{T}_w = \mathbf{H}_{FT}\mathbf{T} \tag{47}$$

The transformation matrices are fixed once the spatial discretizations of the solid and the fluid domains are provided.

3.2 The Coupling Schemes

Two coupling schemes, loosely-coupled and tightly-coupled, are developed for the aerothermoelastic simulation in the HYPATE framework. In the loosely-coupled scheme, the solvers exchange information at the solid-fluid boundary only once at every time step. The loosely-coupled scheme is computationally efficient and maintains accuracy and stability of solution when carefully designed. In the tightly-coupled scheme, at every time step, the solvers exchanges information repeatedly until all the solvers are converged. The tightly-coupled scheme has higher computational cost than the loosely-coupled scheme for each time step. However, it retains the stability of solution at larger time step.

3.2.1 Loosely-coupled scheme

The procedure for the loosely-coupled scheme is illustrated in Fig. 1(a). The steps are as follows,

1. The thermal step:
   (a) Heat flux from the fluid solver is extrapolated,
   $$\dot{\mathbf{q}}^{n+\frac{1}{2},E} = \frac{3}{2}\dot{\mathbf{q}}^{n} - \frac{1}{2}\dot{\mathbf{q}}^{n-1} \tag{48}$$
   (b) The thermal solution $\mathbf{T}$ is updated to step $n+1$, with heat flux $\mathbf{Q}_T^{n+\frac{1}{2}} = \mathbf{H}_{TF}\dot{\mathbf{q}}^{n+\frac{1}{2},E}$
2. The aeroelastic step:
   (a) The thermal solution is passed to the fluid solver and the structural solver, with $\mathbf{T}_w^{n+1} = \mathbf{H}_{FT}\mathbf{T}^{n+1}$.
   (b) The displacement from the structural solver is extrapolated,
   $$\mathbf{u}^{n+1,E} = \mathbf{u}^{n} + \Delta t\left(\frac{3}{2}\dot{\mathbf{u}}^{n} - \frac{1}{2}\dot{\mathbf{u}}^{n-1}\right) \tag{49}$$
   (c) The fluid solutions $\mathbf{p}$ and $\dot{\mathbf{q}}$ are updated to step $n+1$, with displacement $\mathbf{u}_F^{n+1} = \mathbf{H}_{FS}\mathbf{u}^{n+1,E}$

(d) The fluid solution $\mathbf{p}$ is passed to the structural solver.
(e) The structural solution $\mathbf{u}$ is updated to step $n+1$, with aerodynamic loading $\mathbf{F}_S^{n+1} = \mathbf{H}_{SF}\mathbf{p}^{n+1}$

3. Above steps are repeated until end of the simulation.

In step 2e, the aerodynamic loading is fixed, so in the Newton-Raphson procedure for the structural solver, Eqn. (40), the Jacobians of aerodynamic force w.r.t. displacement and velocity are zero.

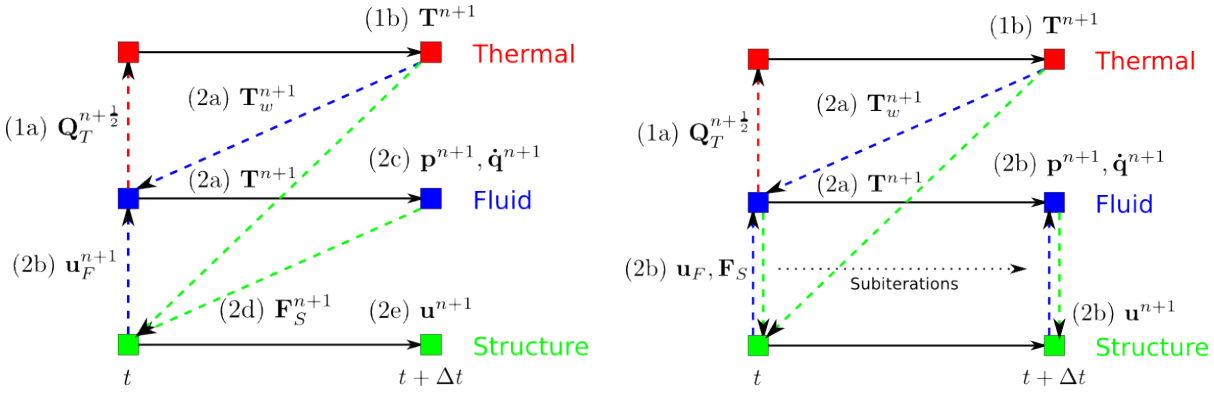

(a) The loosely-coupled scheme. (b) The tightly-coupled scheme.

Figure 1: The schemes for aerothermoelastic simulation.

3.2.2 Tightly-coupled scheme

The procedure for the tightly-coupled scheme is illustrated in Fig. 1(b). The tightly-coupled and the loosely-coupled schemes are the same, except that the aeroelastic step is modified,

(2a) The thermal solution is passed to the fluid solver using Eqn. (45) and the structural solver.
(2b) The fluid and the structural solutions are simultaneously updated to step $n+1$ by solving Eqns. (2), (40), (44), and (46).

Combining Eqns. (2), (40), (44), and (46),

$$\mathcal{R}_S(\mathbf{u}) = \mathbf{F}_S^{n+1} = \mathbf{H}_{SF}\mathbf{p}(\mathbf{H}_{FS}\mathbf{u}, \mathbf{H}_{FS}\dot{\mathbf{u}}) \tag{50}$$

In the Newton-Raphson procedure for the structural solver, the Jacobians of aerodynamic force w.r.t. the structural displacement and velocity are,

$$\frac{\partial \mathbf{F}_S^{n+1}}{\partial \mathbf{u}} = \mathbf{H}_{SF}\frac{\partial \mathbf{p}}{\partial \mathbf{u}_F}\mathbf{H}_{FS} \tag{51}$$

$$\frac{\partial \mathbf{F}_S^{n+1}}{\partial \dot{\mathbf{u}}} = \mathbf{H}_{SF}\frac{\partial \mathbf{p}}{\partial \dot{\mathbf{u}}_F}\mathbf{H}_{FS} \tag{52}$$

In the ROM-based fluid solver, the Jacobians $\frac{\partial \mathbf{p}}{\partial \mathbf{u}_F}$ and $\frac{\partial \mathbf{p}}{\partial \dot{\mathbf{u}}_F}$ can be computed using Eqns. (32) and (33).

3.3 Linearized Stability Analysis

The motivation behind the linearized stability analysis is the disparity of the characteristic times in the thermal and structural solutions in the hypersonic aerothermoelasticity [6]. During a ther-

mal time step, the aerothermoelastic response of a structure can be approximated by the aeroelastic response of a structure with *fixed* temperature distribution [10]. Therefore, the aerothermoelastic stability is represented well by the aeroelastic stability of the heated structure.

The procedure for aeroelastic stability analysis is an extension from the p-method. The stability is determined by solving an eigenvalue problem resulting from the linearization of the structural equation. Based on the assumptions employed, two types of eigenvalue problems, i.e. the polynomial eigenvalue problem (PEP) and the generalized eigenvalue problem (GEP), can be formulated for the linearized stability analysis.

3.3.1 The polynomial eigenvalue problem

To linearize the governing equation for the structural dynamics, Eqn. (36) is perturbed using,

$$\mathbf{u} = \mathbf{u}_{ref} + \Delta\mathbf{u}, \quad \dot{\mathbf{u}} = \dot{\mathbf{u}}_{ref} + \Delta\dot{\mathbf{u}} \tag{53}$$

where $\mathbf{u}_{ref}$, $\dot{\mathbf{u}}_{ref}$, and $\mathbf{T}_{ref}$ are reference states, typically the solution at a given time step. The linearized equation is

$$\mathbf{M}\Delta\ddot{\mathbf{u}} + \mathbf{C}\Delta\dot{\mathbf{u}} + \mathbf{K}\Delta\mathbf{u} = \mathbf{C}_A\Delta\dot{\mathbf{u}} + \mathbf{K}_A\Delta\mathbf{u} \tag{54}$$

where,

$$\mathbf{K} = \frac{\partial\mathbf{F}_I(\mathbf{u}_{ref}, \mathbf{T}_{ref})\mathbf{u}_{ref}}{\partial\mathbf{u}_{ref}}, \quad \mathbf{K}_A = \frac{\partial\mathbf{F}_S(\mathbf{u}_{ref}, \dot{\mathbf{u}}_{ref}, \mathbf{T}_{ref})}{\partial\mathbf{u}_{ref}}, \quad \mathbf{C}_A = \frac{\partial\mathbf{F}_S(\mathbf{u}_{ref}, \dot{\mathbf{u}}_{ref}, \mathbf{T}_{ref})}{\partial\dot{\mathbf{u}}_{ref}} \tag{55}$$

Assume the perturbation is

$$\Delta\mathbf{u} = \tilde{\mathbf{u}}\exp\lambda_p t \tag{56}$$

Combine Eqns. (54) and (56),

$$[\lambda_p^2\mathbf{M} + \lambda_p\tilde{\mathbf{C}} + \tilde{\mathbf{K}}]\tilde{\mathbf{u}} = 0 \tag{57}$$

where symbols $\tilde{\mathbf{C}} = \mathbf{C} - \mathbf{C}_A$ and $\tilde{\mathbf{K}} = \mathbf{K} - \mathbf{K}_A$ are introduced for convenience. The aerodynamic matrices $\mathbf{C}_A$ and $\mathbf{K}_A$ are usually asymmetric, so $\tilde{\mathbf{C}}$ and $\tilde{\mathbf{K}}$ are asymmetric as well.

Equation (57) is a polynomial eigenvalue problem, because it contains both the quadratic and linear terms of the eigenvalue λ_p. The eigenvalues always appear as a complex conjugate pair $\lambda_{p1,2}$,

$$[\lambda_{p1}^2\mathbf{M} + \lambda_{p1}\tilde{\mathbf{C}} + \tilde{\mathbf{K}}]\tilde{\mathbf{u}}_1 = 0, \quad [\lambda_{p2}^2\mathbf{M} + \lambda_{p2}\tilde{\mathbf{C}} + \tilde{\mathbf{K}}]\tilde{\mathbf{u}}_2 = 0 \tag{58}$$

which satisfies,

$$\lambda_{p1} = conj(\lambda_{p2}), \quad \tilde{\mathbf{u}}_1 = conj(\tilde{\mathbf{u}}_2) \tag{59}$$

3.3.2 The generalized eigenvalue problem

The GEP is an approximation of PEP with the following two assumptions,

1. There is no viscous damping, i.e. $\mathbf{C} = 0$.
2. The aerodynamic damping is negligible, i.e. $\mathbf{C}_A = 0$, due to the quasi-steadiness of the aerodynamic loading.

The two assumptions imply that $\tilde{\mathbf{C}} = 0$, and Eqn. (58) simplifies to,

$$[\lambda_{p1}^2\mathbf{M} + \tilde{\mathbf{K}}]\tilde{\mathbf{u}}_1 = 0, \quad [\lambda_{p2}^2\mathbf{M} + \tilde{\mathbf{K}}]\tilde{\mathbf{u}}_2 = 0 \tag{60}$$

Define

$$\lambda_g = -\lambda_{p1}^2 = -conj(\lambda_{p2})^2 \tag{61}$$

and rearrange terms in Eqn. (60),

$$\tilde{\mathbf{K}}\tilde{\mathbf{u}} = \lambda_g\mathbf{M}\tilde{\mathbf{u}} \tag{62}$$

Equation (62) takes the form of the generalized eigenvalue problem in a conventional structural dynamics sense. The difference is that $\tilde{\mathbf{K}}$ is asymmetric, which would result in complex-valued eigenvalues. The eigenvalues of GEP are converted to eigenvalues of PEP by,

$$\lambda_{p1} = \sqrt{-\lambda_g}, \quad \lambda_{p2} = conj(\sqrt{-\lambda_g}) \tag{63}$$

Approximating PEP by GEP is beneficial from a computational aspect. The computational cost of a GEP solution is usually one-tenth of that of a PEP solution.

3.3.3 The stability criteria

The real and imaginary parts of the eigenvalue represent the damping and frequency of the corresponding aeroelastic mode.

$$\zeta = Re(\lambda_p) \tag{64}$$

$$\omega = Im(\lambda_p) \tag{65}$$

The properties of eigenvalues determines the stability of the structure, as provided in Table 1. Two types of instability are identified. When the eigenvalue has a positive real part and a nonzero imaginary part, the corresponding aeroelastic mode represents flutter instability, which is driven by the aerodynamic loading. When the eigenvalue is a positive real, the corresponding aeroelastic mode represents divergence, which is driven by the thermal force in the structure.

$\zeta < 0, \omega \neq 0$	Stable
$\zeta = 0, \omega \neq 0$	Neutrally stable
$\zeta > 0, \omega \neq 0$	Unstable (flutter)
$\omega = 0$	Unstable (divergence)

Table 1: Stability criteria for the linearized stability analysis

4 VERIFICATION OF THE FRAMEWORK

4.1 The ROM-based Fluid Solver

4.1.1 Aerothermoelastic response of a 2D panel

The configuration for the 2D panel is shown in Fig. 2. The panel is simply supported at the leading and trailing edges. The geometrical parameters are $h = 2.5\text{mm}$ and $a = 1\text{m}$. The flight conditions are $M_\infty = 4.0$, $p_\infty = 2087.2\text{Pa}$, and $T_\infty = 266.7\text{K}$. The material properties are temperature dependent [26]. At initial temperature ($T = 300K$), $\rho = 2768.1\text{kg/m}^3$, $E = 72.86\text{GPa}$, $\nu = 0.325$, $\alpha = 2.236 \times 10^{-5}/\text{K}$, $\kappa^s = 132.05\text{W/mK}$, and $c = 850.99\text{J/kgK}$. Three cases are considered. In case I, the low-fidelity fluid solver is used. In cases II and III, the

ROM-based fluid solver is used. The data for generating the ROM is from the analytical models, so the results from the two cases should be identical. In cases I and II, the loosely-coupled scheme is used to compute the transient aerothermoelastic response with a time step of 5ms. In case III, the tightly-coupled scheme is used to compute the quasi-steady aerothermoelastic response with a time step of 50ms.

The transient solutions, i.e. those from cases I and II and Ref. [27], and the quasi-steady solution from case III are compared in Figs. 3(a)-3(d). Figure 3(a) illustrates the mid-panel displacement nondimensionalized by thickness. The panel undergoes a thermally-driven response, which causes the panel to buckle into the flow. At the stability boundary near $t = 2.1s$, snap-through occurs, and the panel buckles out of the flow. The transient solutions are identical up to the stability boundary. The quasi-steady solution is able to capture the trend of the transient responses and predicts the identical stability boundary. The average pressure on the panel surface is shown in Fig. 3(b). The loadings in the transient solutions agree well with each other. The quasi-steady loading is lower than the transient counterparts, because the structural velocity, and hence the unsteady component of the aerodynamic force, are neglected in the quasi-steady solution. The average panel temperature is shown in Fig. 3(c). The transient and quasi-steady solutions are identical. The average heat flux on the panel surface is shown in Fig. 3(d). The transient and quasi-steady solutions agree well with each other, except the ROM-based heat flux is slightly higher than the heat flux from analytical model (less than 1%).

The comparisons verifies,

1. The correctness of the transient aerothermoelastic responses using the HYPATE framework.
2. The correctness of the ROM-based fluid solver.
3. The feasibility of the quasi-steady approximation of the structural response.

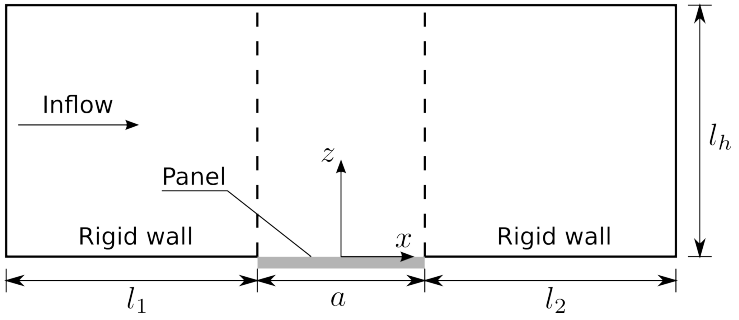

Figure 2: The configuration of a 2D panel.

4.1.2 ROM corrections and scaling

To verify and demonstrate the capability of the novel method for ROM correction and scaling (Eqn. 28), a CFD-based ROM was generated for the panel configuration from the previous section. The baseline case has a uniform wall temperature $T_{ref} = 300K$, and a typical deformation described by 3 sinusoidal modes with modal amplitudes $[a_1, a_2, a_3] = [1, -0.35, -0.1]h$. The ROM correction and scaling method is tested for three cases ordered in increasing complexity, and compared against CFD results:

1. Case I: correction for non-uniform wall temperature,

$$T_w(x) = T_{ref}(1.25 - 0.5x/a + 0.1\sin(3\pi x/a)) \tag{66}$$

2. Case II: case I plus correction for change in flight conditions, $M_\infty = 4.5, p_\infty = 2500$Pa
3. Case III: case II plus correction for change in geometrical scale, $\xi = 5$

The corrected and scaled ROM results, in the form of dimensional pressure and heat flux, are shown in Figure 4 as a function of panel streamwise axis. Each case is compared to a corresponding CFD result appearing in a dashed line, and the relative L2 error is indicated in the legend. Small errors, between 0.4% and 6.7% are obtained, although the conditions for the cases considered here are quite different than the conditions of the original ROM. This highlights and verifies the effectiveness of the novel correction developed in the current study.

4.2 The Linearized Stability Analysis

4.2.1 Aeroelastic response of a 3D panel

The first example is the aeroelastic response of a 3D panel, shown in Fig. 5(a), simply supported along its edges. The geometrical parameters are $a/h = 500$ and $a/b = 1$. The material properties are $\nu = 0.3$ and $\alpha = 1.2 \times 10^{-6}/\text{K}$. The mass ratio $\mu_s = 5.355 \times 10^{-4}$. The aerodynamic loads are obtained using the piston theory. Two cases with different temperature increments are considered: (1) $\Delta T = T_{cr}$, (2) $\Delta T = 2T_{cr}$.

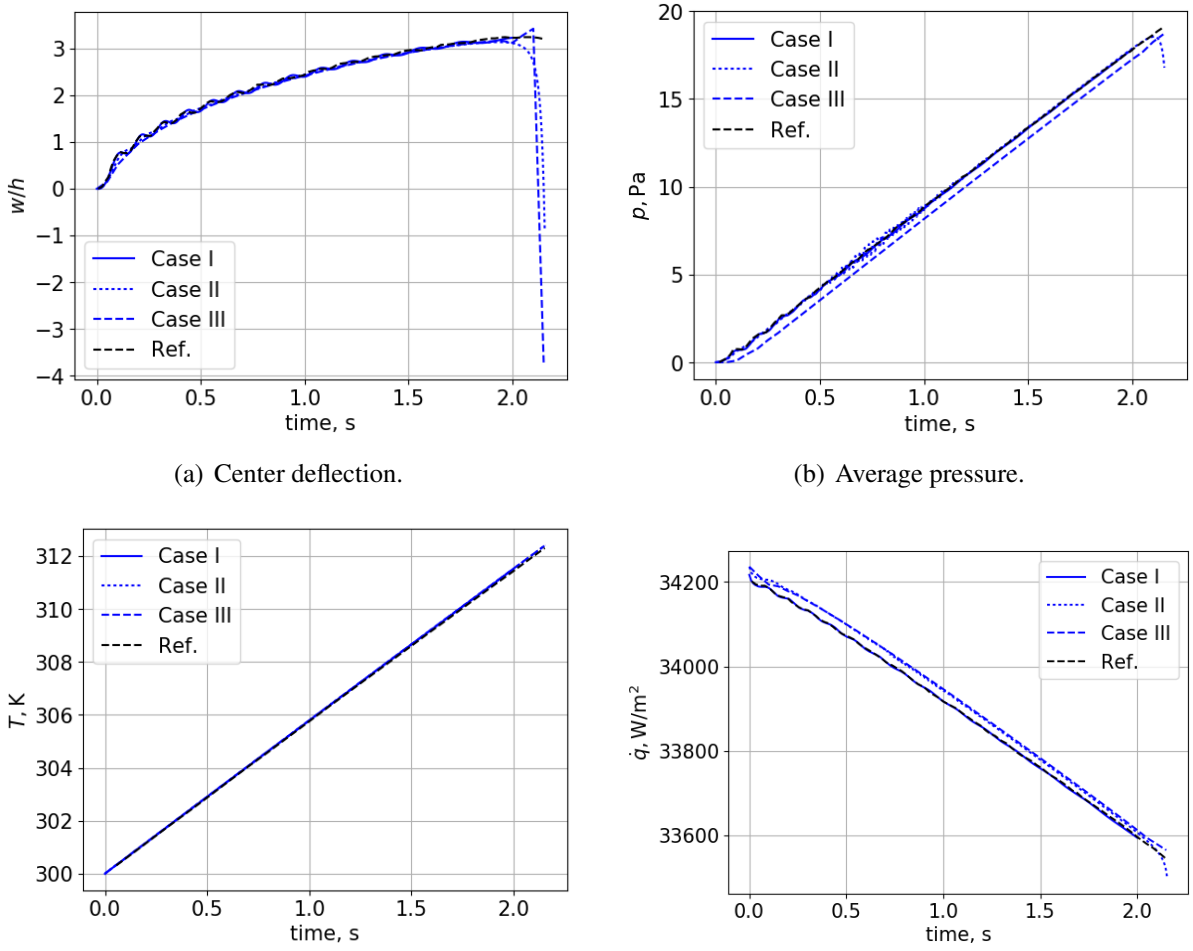

(a) Center deflection.

(b) Average pressure.

(c) Average temperature.

(d) Average heat flux.

Figure 3: The aerothermoelastic response of the 2D panel.

The first set of results are obtained directly from temporal responses of the panel, as shown in Fig. 5(b). The amplitudes of limit cycle oscillation (LCO) are computed at a series of dynamic pressures. At each dynamic pressure, the aeroelastic simulation is run for 5000 time steps so that the time response enters a stable state or a LCO state. The results are compared with those from the literature (Nydick et al. [28] and Dowell [29]).

In general, the results from current study agree well with those from literature. The flutter points predicted by HYPATE are $\tilde{\lambda} = 344.0$ for $\Delta T = T_{cr}$ and $\tilde{\lambda} = 191.1$ for $\Delta T = 2T_{cr}$. Compared with the literature results, the errors are less than 1%. Moreover, the case $\Delta T = 2T_{cr}$ provides an illustration of three typical types of panel response [30]. The panel response is controlled by two types of forces, i.e. the thermally-induced inplane compressive force and the aerodynamic

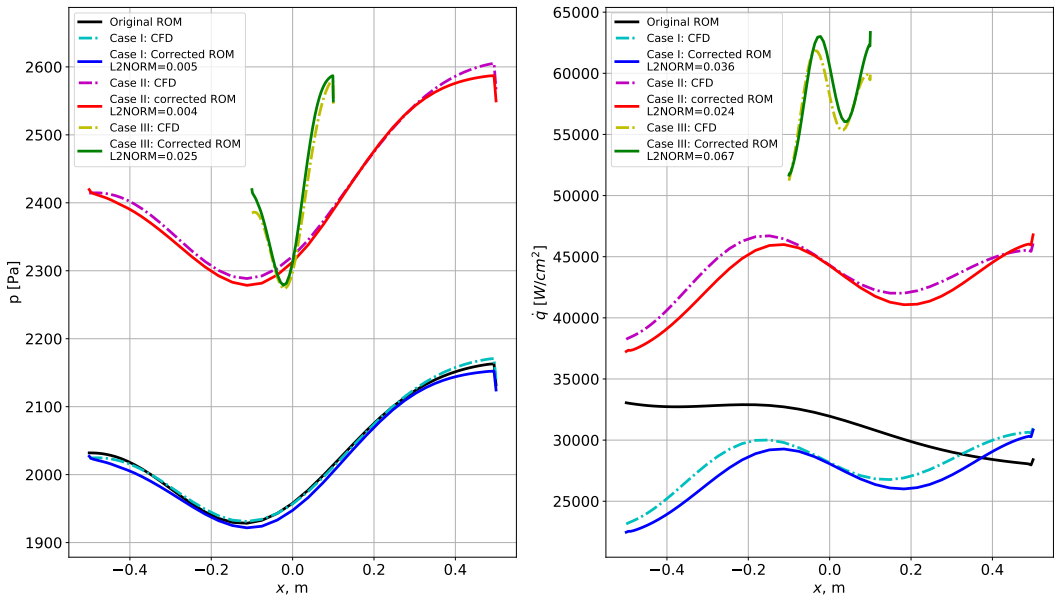

Figure 4: Verification of ROM correction and scaling

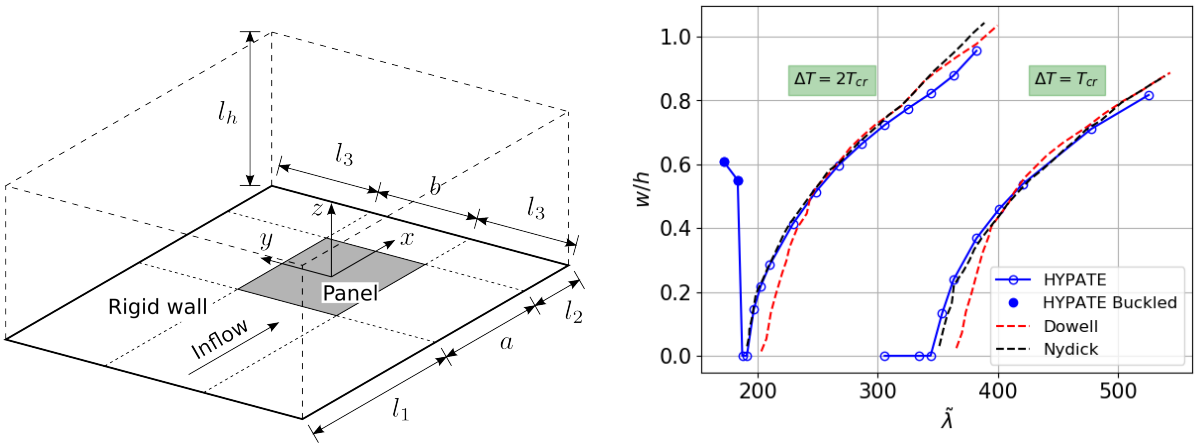

(a) The geometrical configuration.

(b) The LCO curves.

Figure 5: Aeroelastic response of a 3D panel

force. When the dynamic pressure is low ($\tilde{\lambda} < 183.5$), the aerodynamic force is weaker than the compressive force and type I response occurs: The panel is thermally buckled but dynamically stable, as illustrated in Fig. 6(a). As the dynamic pressure increases ($183.5 < \tilde{\lambda} < 191.1$), The two forces are both moderate and type II response occurs: The panel is stabilized and has zero LCO amplitude, as illustrated in Fig. 6(b). After the flutter point ($\tilde{\lambda} > 191.1$), the aerodynamic force becomes stronger than the compressive force and the panel enters the LCO state.

The second set of results are obtained from the LSA using the PEP and GEP formulations. The frequencies ω and dampings ζ of the first six aeroelastic modes are computed at a series of dynamic pressures. The first two modes are found to be the source of instability and the higher modes are stable. In this section, the frequencies and dampings are nondimensionalized by

$$\bar{\omega} = \frac{\omega}{\omega_o}, \quad \bar{\zeta} = \frac{\zeta}{\omega_o} \tag{67}$$

where ω_o is the natural frequency of the first structural mode of the unheated panel.

Figure 7(a) illustrates the LSA results for the first case ($\Delta T = T_{cr}$). The frequencies of the two modes coalesce as the dynamic pressure increases. When the frequencies coalesce, the damping of one of the modes becomes positive, and the other becomes negative, indicating a flutter-type instability. The flutter point is $\tilde{\lambda} = 343.3$, within 1% error compared with results from time-domain analysis.

Figure 7(b) illustrates the LSA results for the second case ($\Delta T = 2T_{cr}$). The flutter point is $\tilde{\lambda} = 190.9$, where the damping becomes positive. Furthermore, the LSA results capture the two types of panel response before the flutter point. When $\tilde{\lambda} < 183.4$, mode 1 has zero frequency and positive damping, indicating that the panel has divergence-type instability, which corresponds to the type I response in the time-domain analysis. When $183.4 < \tilde{\lambda} < 190.9$, the modes have negative damping and the panel is stable, which corresponds to the type II response.

In Figs. 7(a) and 7(b), the PEP and GEP formulations produce almost identical results. The maximum error in the frequencies is less than 0.1%. Compared with PEP results, the damping computed by GEP is "shifted" upward by a small amount, typically 1% of the reference frequency. The shift in damping is caused by neglecting the aerodynamic damping matrix due

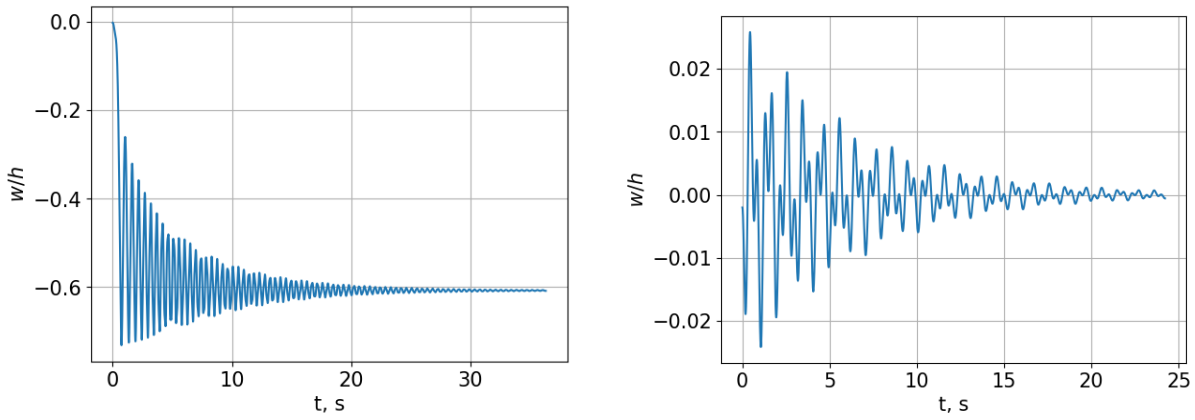

(a) Type I response at $\tilde{\lambda} = 172.0$.

(b) Type II response at $\tilde{\lambda} = 187.3$.

Figure 6: Typical panel responses before flutter when $\Delta T = 2T_{cr}$.

to the quasi-steady assumption. The changes in the flutter points due to the shift are negligible. The comparison between PEP and GEP results justifies the quasi-steady assumption in the hypersonic flow regime. Also, the results indicate that the positive damping in flutter-type instablity is mainly introduced by the aerodynamic stiffness matrix.

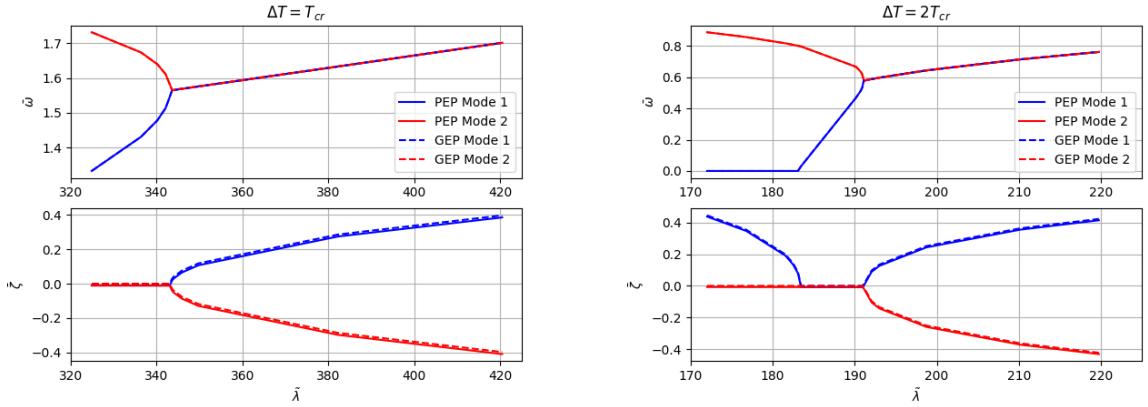

(a) Case 1: $\Delta T = T_{cr}$. (b) Case 2: $\Delta T = 2T_{cr}$.

Figure 7: The linearized stability analysis results (PEP v.s. GEP).

4.2.2 Aerothermoelastic response of a 2D panel

The second verification is a continuation from the 2D panel case from Section 4.1.1. The LSA using the PEP and GEP formulations are applied to aerothermoelastic responses with the ROM-based fluid solver. In the first case, the transient response with a time step of 5ms is considered, and in the second case, a quasi-steady response with a time step of 50ms is examined.

The PEP and GEP results from the first case are compared in Fig. 8(a), where the first aeroelastic mode is examined. The frequency is decreasing with intermittent fluctuation. The frequency gradually reaches zero as the system approaches the stability boundary. The identified stability boundary is 1.985s, which agrees with the time-domain analysis. After the stability boundary, the frequency becomes zero and the damping becomes positive, indicating a divergence type of instability. That means the instability of the panel is driven by the thermally-induced inplane force. The frequencies computed from PEP are identical to those from GEP. The dampings computed from PEP and GEP differ by a small quantity (1% of the reference frequency), due to the neglected aerodynamic damping matrix. Like the flutter-type instablity, the positive damping in divergence-type instablity is mainly due to the aerodynamic stiffness matrix.

The GEP results from the first and the second cases are compared in Fig. 8(b). The frequency extracted from the quasi-steady solution varies smoothly with time, and follows the decreasing trend of the transient solution well. The predicted stability boundary is 2.1s, which agrees with the corresponding time-domain solution. The difference with the prediction from the transient results is attributed to the differences in the time step. Therefore, the quasi-steady aerothermoelastic response is shown to be a fast and acceptable approximation of its transient counterpart. The quasi-steady solution takes only one-tenth of the time steps required by the transient solution.

5 APPLICATION TO AEROTHERMOELASTIC SCALING LAWS

5.1 Background on Classical Aerothermoelastic Scaling

During the last five decades aeroelastically scaled wind tunnel models have been widely used and played an important role in aeroelasticity, since aeroelastic scaling laws allowed one to relate small-scale wind tunnel test results to the behavior of a full-scale system. Such scaling laws are based on dimensional analysis of the governing equations to establish scaling parameters used for designing aeroelastically scaled models [31]. This approach is integrated in the Transonic Dynamic Tunnel at NASA Langley Research Center, which is a dedicated facility for testing aeroelastically scaled models [32]. However, the effect of kinetic heating is not generally simulated by current wind tunnel testing technologies. The presence of kinetic heating can influence the aeroelastic behavior primarily by reduction in stiffness due to degradation of material properties with temperature combined with a reduction due to an unfavorable stress distribution associated with thermal expansion. A few attempts have been made in the past to incorporate thermal effects into the aeroelastic scaling laws, resulting in aerothermoelastic scaling laws [2, 33]. These conlcuded that complete similarity is impossible to achieve for scale ratios that differ from unity. The similarity parameters that need to be satisfied are derived from a proper non-dimensionalization of the general equations for stress, displacement and temperature distribution of a body immersed in a hot, flowing gas. The parameters for the general case of complete aerothermoelastic similarity, as derived in Ref. [2] Eqn. (52), are given in Table 2.

(I)	$M_\infty,\ Re_\infty, \frac{\rho V_\infty^2}{E_{ref}},\ \frac{\kappa^g_\infty}{\kappa^s_{ref}},\ \alpha_{ref}T_{ref},\ \frac{\rho_s}{\rho}$
(II)	$\frac{T_{ref}}{T_\infty},\ \frac{\kappa^g_{ref}t_{ref}}{L^2},\ \frac{V_\infty t_{ref}}{L},\ \frac{u_{ref}}{L},\ \frac{\sigma_{ref}}{E_{ref}},\ \frac{T_w^{init}}{T_{ref}}$
(III)	$\frac{\epsilon\sigma_B T^3_{ref}L}{\kappa^s_{ref}},\ \frac{\rho_s g L}{\rho V_\infty^2},\ \frac{p_{ext}}{E_{ref}}$
(IV)	$Pr,\ \gamma,\ \nu,\ \hat{\kappa}^g,\ \hat{c}^g_p, \hat{\mu},\ \hat{\kappa}^s,\ \hat{c}^s_p,\ \hat{E}, \hat{\alpha},\ \hat{\epsilon}_w$

Table 2: Scaling parameters for complete aerothermoelastic similarity

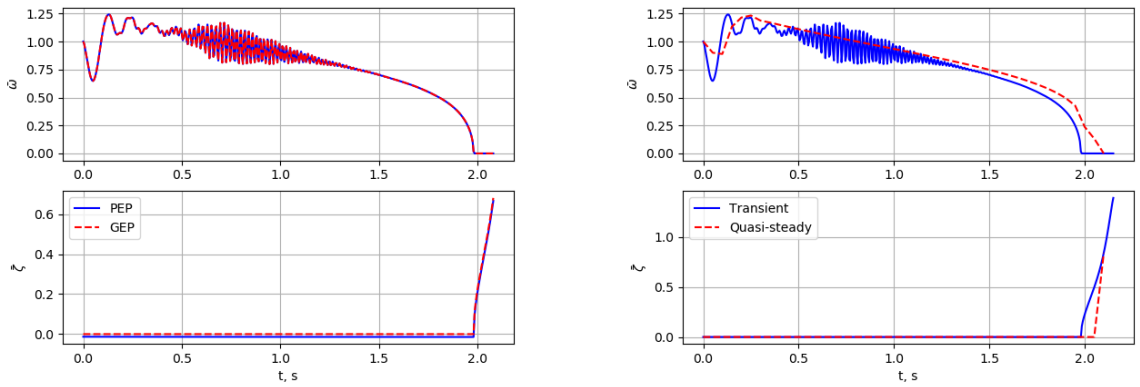

(a) The PEP and GEP formulations.

(b) The transient and quasi-steady responses.

Figure 8: The damping and frequency in the aerothermoelastic response.

The primary similarity parameters are given in the top line, and satisfying all of them presents a major conflict. The ratio of densities $\frac{\rho_s}{\rho}$ is only required for dynamic aerothermoelastic problems, and may be ignored for large ratios [2]. The parameters in line (II) define a reference state for temperature T_{ref}, time t_{ref}, deflection u_{ref}, stress σ_{ref}, and the initial wall temperature T_w^{init}. The first two parameters of line (III) are required for cases where significant surface radiation and gravity effects are present, and the third parameter represents the scaling of non-aerodynamic loadings. Finally, the parameters in line (IV) relate to similarity of gas and material properties. The parameters with $\hat{\square}$ are temperature dependent.

One approach to deal with this basic conflict is by examining more restricted situations, instead of the general problem, such that simplifying assumptions can be made and some of the parameters can be relaxed. Considering the restricted case of thin and flat panels in supersonic flow, there is no longer a separate Mach number requirement as long as the Mach number is supersonic ($M_\infty > 1.7$), and the effect of the thickness ratio $\tau = h/L$ may be neglected since only the deformation affects the loading [2]. This allows a variation of Mach and τ in the scaling process. In addition, the heat flux may be approximated by boundary layer analytical solutions for flat plates, which facilitates the grouping of some parameters. Furthermore, a uniform through-thickness temperature rise can be assumed, and the heat conduction in the plane of the panel may be neglected. These assumptions allow more flexibility in the scaling, reducing the similarity parameters listed in Table 3, as derived in Ref. [2], Eqn. (70).

(I)	$\frac{\rho V_\infty^2}{E_{ref} M_\infty \tau^3}$, $\frac{\rho_s M_\infty \tau}{\rho}$, $\frac{\alpha_{ref}(T_{ref}-T_w^{init})}{\tau^2}$, $\eta = \frac{\kappa^g Re_\infty^{0.8} Pr^{1/3} t_{ref}}{\rho_s c_p^s L^2 \tau}$
(II)	$\frac{T_{ref}-T_w^{init}}{T_{AW}-T_w^{init}}$, $\frac{V_\infty t_{ref}}{L}$, $\frac{u_{ref}}{L\tau}$, $\frac{\sigma_{ref}}{E_{ref}\tau^2}$
(III)	$\frac{\epsilon \sigma_B L T^4}{\kappa^g Re_\infty^{0.8} Pr^{1/3}(T_{ref}-T_w^{init})}$, $\frac{\rho_s g L M_\infty}{\rho V_\infty^2}$, $\frac{p_{ext}}{E_{ref}\tau^4}$
(IV)	ν, $\hat{\kappa}^g$, $\hat{c}_p^g$, $\hat{\mu}$, $\hat{\kappa}^s$, $\hat{c}_p^s$, $\hat{E}$, $\hat{\alpha}$, $\hat{\epsilon}_w$

Table 3: Reduced set of scaling parameters for aerothermoelastic similarity of thin panels in supersonic flow

The first parameter in the top line of Table 3 is the non-dimensional dynamic pressure $\tilde{\lambda}$, the basic panel flutter parameter. The second parameter is the mass ratio μ_s, and can be usually ignored if it is large enough. The third parameter relates to thermal stresses similarity, and defines the initial wall temperature T_w^{init}. The fourth parameter η is a grouping of several parameters related to heat transfer and defines the thermal time t_{ref}. While a more flexible scaling requirement is provided by the set reduced parameters in Table 3, it is still difficult to satisfy them, particularly when the Mach number increases. The challenges associated with scaled aerothermoelastic testing have resulted in the use of "incomplete" aerothermoelastic testing and "restricted purpose" testing approaches. "Incomplete" aerothermoelastic testing refers to the usage of additional means other than aerodynamics to provide loading or heating. This requires a priori knowledge of the loading and heating on the full-scale vehicle, as well as the ability to accurately apply these loads at the appropriate locations as a function of time, which is difficult to achieve in practice. "Restricted purpose" testing implies a study of the aerothermoelastic problem assuming that the coupling between the aerodynamic pressure, aerodynamic heating, heat conduction and stress-deflection phenomena is weak. However, the fluid-thermal-structural

interactions cannot be decoupled in modern hypersonic vehicles since they are based on an integrated airframe-propulsion concept, which strengthens the interactions between the various components [10].

5.2 Refined Aerothermoelastic Scaling Procedure

As indicated in the previous section, the classical approach to aerothermoelastic scaling is inadequate for modern applications and leads to the conclusion that scaled aerothermoelastic testing appears to be intractable [2]. An alternative approach to aerothermoelastic scaling is explored in this study. The approach is based on a combination of the classical approach and a numerical simulation of the specific problem being considered. This two-pronged approach for generating aerothermoelastic scaling laws is illustrated in Fig. 9. The left hand branch depicts the classical approach used in [2]. The innovative approach developed here combines the classical approach with aerothermoelastic numerical simulation as represented by the right hand branch. Using such aerothermoelastic numerical simulations, one can obtain a complete solution, such that the aerothermoelastic stability boundary, for the prototype (i.e. full scale) as well as the scaled model. From the comparison and adjustment of these two stability boundaries the scaling laws for the specialized cases can be obtained without recourse to the ad-hoc assumptions used the classical approach. For more complex configurations, such as a complete hypersonic vehicle, this adjustment process can formulated as a constrained optimization problem, where the design variables can be selected to correspond to the most important parameters needed for the refined simulation that differ from those employed when generating the model based on classical similarity. This approach was used in [3], and was found to be effective.

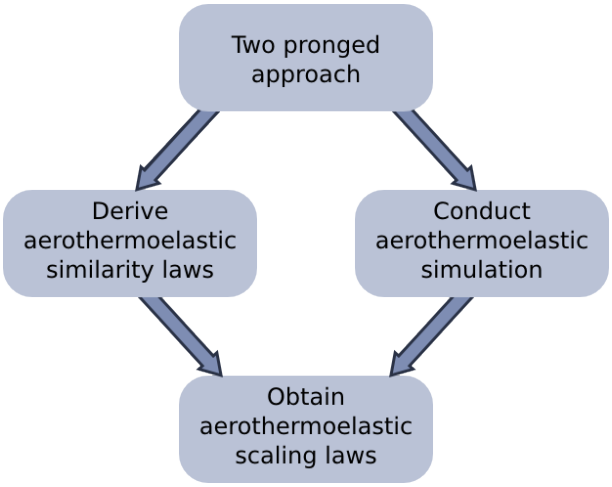

Figure 9: Schematic description of two-pronged approach for developing aerothermoelastic similarity laws

5.3 Refined Aerothermoelastic Scaling Test Case

A “realistic” 3D panel configuration in hypersonic flight was chosen for the demonstration of the scaling approach developed together with the efficient capability to simulate and identify instabilities for extended flight times. The parameters for the test case are provided in Table 4. Although hypersonic vehicles typically flies at high altitudes, a rather low altitude of 20km was chosen. This is for reducing the computational effort by decreasing the time when instability occurs from hours to minutes.

For a simplified demonstration, an “ideal” case is considered where: (1) the wind tunnel is capable of simulating the same gas properties as in flight, and (2) the model is built from the same

a, b	0.5m
h	8mm
Front plate length, L_f/a	1.0
Material	Aluminum-7075-T651 [26]
M_∞	6.0
Altitude	20km
Incidence angle, θ	2.5^o

Table 4: Refined aerothermoelastic scaling test case parameters

material as the prototype. As indicated earlier, the first step in the new approach is to consider the classical parameters on the left-hand branch in Fig. 9. For this case, when neglecting radiation and gravity effects, all the similarity parameters in Table 3 are satisfied, except the heat transfer parameter η.

In the next step, the refined approach represented by the right-hand branch in Fig. 9 is implemented by performing numerical simulations for the prototype and scaled models. Aerothermoelastic numerical simulations were performed for different geometrical scaling between $\xi = 1$ (full-scale) and $\xi = 10$ to identify the variation of the time t_I, when the system becomes unstable, as a function of the geometrical scale. The scaling results from both the classical and the refined approaches are shown in Fig. 10.

In the classical approach, the time when the instability occurs t_I and the characteristic length are related by,

$$\frac{t_I V_\infty}{L} = const \tag{68}$$

where V_∞ is assumed to be constant for the case considered here. The relation between t_I and the geometrical scale ξ is determined from Eqn. (68),

$$\frac{t_I}{t_{I,ref}} = \frac{L}{L_{ref}} = \frac{1}{\xi} \tag{69}$$

which implies that the time for onset of instability t_I is inversely proportional to the geometrical scale ξ.

In the refined approach, as the geometrical scale increases, the time t_I of the scaled model is lower than the value predicted by the classical approach. The discrepancy is due to the mismatch of the heat transfer similarity parameter η, which increases as the characteristic length decreases. The increase of η leads to the increase in the heat flux, resulting in a faster degradation of material properties and earlier onset of instability.

The final step of the new approach is adjustment of the parameters to obtain matching between the full-scale and scaled stability boundaries. This is a complicated task that requires solving a constrained optimization problem with model and gas properties as design variables. For the particular case considered here, where the material properties for the model and the gas properties are identical, one can identify a single design variable that can be adjusted to permit matching the stability boundaries. By recognizing that the heat flux reduction required can be obtained by scaling the upstream plate length L_f/a independently from the geometrical scale; allows one to select a larger upstream plate length thus reducing the heat flux acting on the panel. This modification also changes boundary layer thickness ratio δ/a for the approaching

flow. However, at the high Reynolds numbers are considered, δ/a has only a secondary effect on loading. The scaled time t_I as a function of upstream plate length is shown in Fig. 11(a) for different geometrical scales. It is evident that a longer upstream plate length extends the time t_I, and thus a given geometrical scale can be adjusted for similarity with the prototype. The required upstream plate length for similarity was interpolated and is presented as function of geometrical scale in Fig. 11(b). The required plate length was expected to increase monotonically with geometrical scale, as greater heat flux reduction is required for models of a smaller scale. However, the required plate length reaches a maximum of ~ 2.3 at $\xi = 7$ and then decreases for larger geometrical scales. This effect is due to the fact that heat conduction, which was neglected in the analytical approach, becomes more pronounced at smaller scales. This demonstrates how numerical simulation may be used to augment the scaling requirements.

6 CONCLUDING REMARKS

This study examines the issue of aerothermoelastic scaling employing an advanced and efficient framework for aerothermoelastic simulation. The principal findings of the study are summarized below.

1. A new ROM correction and scaling method was developed. It is able to account for both non-uniform temperature distribution and extrapolation to different flow conditions or geometrical scales. Thus, it expands the applicability of a certain ROM to a wider range of applications and dramatically reduces the cost for ROM generation.
2. A new computational approach combining the linearized stability analysis and a tightly-coupled scheme were developed for efficient and automatic identification of aerothermoelastic stability boundary. This new approach allows one to use a large time step size in the aerothermoelastic simulation, and it is suitable for simulation of extended flight time

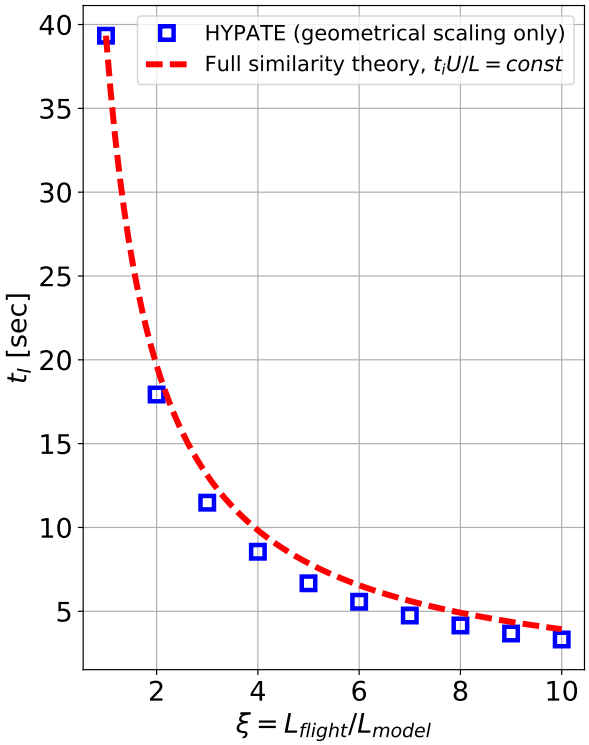

Figure 10: Panel instability time vs. geometrical scaling

along the trajectory of a hypersonic vehicle.

3. A new, two-pronged approach to aerothermoelastic scaling is implemented. It combines the classical scaling approach with augmentation from numerical simulations of the specific problem. The new approach was applied for scaling a 3D panel configuration in hypersonic flow for an "ideal" case where the model and the prototype are built of the same material and tested in a gas with identical properties. Similarity between the prototype and a range of small-scale models was successfully obtained by adjusting a single variable consisting of the upstream plate length.

The aerothermoelastic scaling approach described in this study can be eventually applied to testing components of a hypersonic vehicle. Furthermore, the approach can be also used to map aerothermoelastic results obtained in a full scale test on an actual vehicle to a vehicle having different geometric size. Therefore, it has the potential for saving considerable funds in the process of developing a hypersonic vehicle.

ACKNOWLEDGEMENT

The authors would like to acknowledge the help of Professor Jack J. McNamara from The Ohio State University.

7 REFERENCES

[1] McNamara, J. J. and Friedmann, P. P. (2011). Aeroelastic and aerothermoelastic analysis in hypersonic flow: Past, present, and future. *AIAA Journal*, 49(6), 1089–1122.

[2] Dugundji, J. and Calligeros, J. M. (1962). Similarity laws for aerothermoelastic testing. *Journal of the Aerospace Sciences*, 29(8), 935–950.

[3] Friedmann, P. (2004). Aeroelastic scaling for rotary-wing aircraft with applications. *Journal of Fluids and Structures*, 19(5), 635–650.

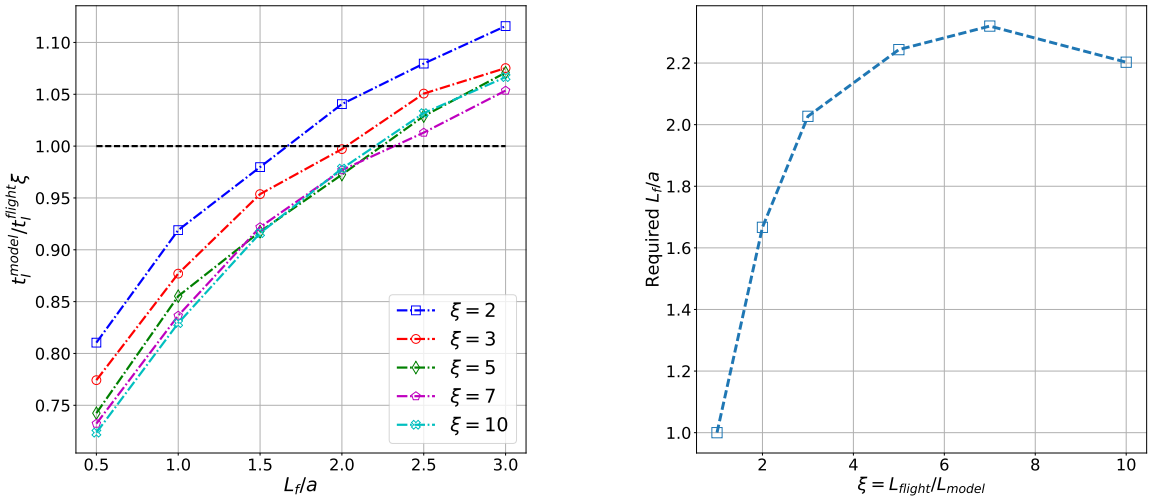

(a) Panel instability time vs. front plate length

(b) Required front plate length for similarity.

Figure 11: Panel instability time similarity by front plate length adjustment

[4] Huang, D. and Friedmann, P. P. (2016). An integrated aerothermoelastic analysis framework for predicting the response of composite panels. In *AIAA 2016-1090, 15th Dynamics Specialists Conference*. San Diego, CA, pp. 1–37.

[5] Huang, D., Rokita, T., and Friedmann, P. P. (2017). An aerothermoelastic analysis framework enhanced by model order reduction with applications. In *AIAA 2017-1601, 58th AIAA/ASCE/AHS/ASC Structures, Structural Dynamics, and Materials Conference*. Grapevine, TX, pp. 1–19.

[6] Culler, A. J. and McNamara, J. J. (2011). Impact of fluid–thermal–structural coupling on response prediction of hypersonic skin panels. *AIAA Journal*, 49(11), 2393–2406.

[7] Crowell, A. R., McNamara, J., and Miller, B. (2011). Hypersonic aerothermoelastic response prediction of skin panels using computational fluid dynamic surrogates. *Journal of Aeroelasticity and Structural Dynamics*, 2(2).

[8] Falkiewicz, N. J., S. Cesnik, C. E., Crowell, A. R., et al. (2011). Reduced–order aerothermoelastic framework for hypersonic vehicle control simulation. *AIAA Journal*, 49(8), 1625–1646.

[9] Crowell, A. R. and McNamara, J. J. (2012). Model reduction of computational aerothermodynamics for hypersonic aerothermoelasticity. *AIAA Journal*, 50(1), 74–84.

[10] Lamorte, N., Friedmann, P. P., Dalle, D. J., et al. (2014). Uncertainty propagation in integrated airframe–propulsion system analysis for hypersonic vehicles. *Journal of Propulsion and Power*, 31(1), 54–68.

[11] Hodges, D. H. and Pierce, G. A. (2011). *Introduction to Structural Dynamics and Aeroelasticity*, vol. 15, chap. 5. Cambridge University Press, pp. 175–200.

[12] Sirovich, L. (1987). Turbulence and the dynamics of coherent structures, part I: Coherent structures. *Quarterly of Applied Mathematics*, 45(3), 561–571.

[13] Forrester, A., Sobester, A., and Keane, A. (2008). *Engineering Design Via Surrogate Modelling: A Practical Guide*. John Wiley & Sons.

[14] Ashley, H. and Zartarian, G. (1956). Piston theory – a new aerodynamic tool for the aeroelastician. *Journal of the Aeronautical Sciences*, 23(12), 1109–1118.

[15] Crowell, A. R., McNamara, J. J., Kecskemety, K. M., et al. (2015). A reduced order aerothermodynamic modeling framework for hypersonic aerothermoelasticity. In *AIAA Paper 2010-2969, 51th AIAA/ASCE/AHS/ASC Structures, Structural Dynamics, and Materials Conference*. pp. 1–22.

[16] Eckert, E. R. G. (1960). Survey of boundary layer heat transfer at high velocities and high temperatures. Tech. rep., Minnesota. Univ., Minneapolis. Heat Transfer Lab.

[17] Crowell, A. R., Miller, B. A., and McNamara, J. J. (2014). Robust and efficient treatment of temperature feedback in fluid–thermal–structural analysis. *AIAA Journal*, 52(11), 2395–2413.

[18] Chapman, D. R. and Rubesin, M. W. (1949). Temperature and velocity profiles in the compressible laminar boundary layer with arbitrary distribution of surface temperature. *Journal of the Aeronautical Sciences*, 16(9), 547–565.

[19] Edwin van der Weide, Kalitzin, G., Schluter, J., et al. (2006). Unsteady turbomachinery computations using massively parallel platforms. In *AIAA Paper 2006-0421, 44th AIAA Aerospace Sciences Meeting and Exhibit*. pp. 1–16.

[20] Chung, J. and Hulbert, G. M. (1993). A time integration algorithm for structural dynamics with improved numerical dissipation: The generalized–α method. *Journal of Applied Mechanics*, 60(2), 371–375.

[21] Newmark, N. M. (1959). A method of computation for structural dynamics. *Journal of the Engineering Mechanics Division*, 85(3), 67–94.

[22] Hilber, H. M., Hughes, T. J. R., and Taylor, R. L. (1977). Improved numerical dissipation for time integration algorithms in structural dynamics. *Earthquake Engineering & Structural Dynamics*, 5(3), 283–292.

[23] Hughes, T. J. (1987). *The Finite Element Method: Linear Static and Dynamic Finite Element Analysis*, chap. 8. Englewood Cliffs, New Jersey: Prentice Hall, pp. 459–478.

[24] Farhat, C., Lesoinne, M., and Le Tallec, P. (1998). Load and motion transfer algorithms for fluid/structure interaction problems with non–matching discrete interfaces: Momentum and energy conservation, optimal discretization and application to aeroelasticity. *Computer Methods in Applied Mechanics and Engineering*, 157(1–2), 95–114.

[25] Jaiman, R. K., Jiao, X., Geubelle, P. H., et al. (2006). Conservative load transfer along curved fluid–solid interface with non–matching meshes. *Journal of Computational Physics*, 218(1), 372–397.

[26] U.S. Department of Defence (1998). *Military Handbook, MIL–HDBK–5J: Metallic Materials and Elements for Aerospace Vehicle Structures*. U.S. Department of Defence, pp. 3368–3426.

[27] LaFontaine, J. H., Gogulapati, A., Miller, B. A., et al. (2015). Effects of strain hardening on fluid–thermal–structural interactions. In *AIAA Paper 2015-1629, 56th AIAA/ASCE/AHS/ASC Structures, Structural Dynamics, and Materials Conference*. Kissimmee, FL, pp. 1–17.

[28] Nydick, I., Friedmann, P. P., and Zhong, X. (1995). Hypersonic panel flutter studies on curved panels. In *AIAA Paper 95-1485-CP, Proceedings of 34th AIAA/ASME/ASCE/AHS/ASC Structures, Structural Dynamics, and Materials Conference*. New Orleans, LA, pp. 2995–3011.

[29] Dowell, E. H. (1966). Nonlinear oscillations of a fluttering plate. *AIAA Journal*, 4(7), 1267–1275.

[30] Dowell, E. H. and Ilgamov, M. (1988). *Studies in Nonlinear Aeroelasticity*. New York: Springer-Verlag, pp. 163–186.

[31] Bisplinghoff, R. L., Ashley, H., and Halfman, R. L. (1955). *Aeroelasticity*. Addison-Wesley Publishing Company.

[32] Ivanco, T. G. (2013). Unique testing capabilities of the NASA Langley transonic dynamics tunnel, an exercise in aeroelastic scaling. In *AIAA 2013-2625, Ground Testing Conference*. pp. 1–23.

[33] Molyneux, W. (1962). A consideration of the similarity requirements for aerothermoelastic test on reduced scale models. Tech. rep., Ministry of Aviation, Royal Aircraft Establishment, RAE Farnborough.

COPYRIGHT STATEMENT